Surface diffusion dewetting of thin solid films: Numerical method and application to Si/SiO_2

E. Dornel,* J-C. Barbé, F. de Crécy, and G. Lacolle
CEA-DRT-LETI - CEA/GRE- 17, rue des Martyrs, 38054 Grenoble cedex 9, France

J. Eymery
Équipe mixte CEA-CNRS-UJF, Nanophysique et Semiconducteurs, CEA/DRFMC/SP2M, 17, rue des Martyrs, 38054 Grenoble cedex 9, France

(Received 18 October 2005; revised manuscript received 30 January 2006; published 27 March 2006)

A method has been developed to calculate and use a surface chemical potential which is valid in the large curvature regime for any surface energy function. It is applied to the solid-phase dewetting of a finite film with an initial rectangular profile and considers the surface diffusion mechanism. For an isotropic surface energy, the film aspect ratio and the adhesion energy between the film and the substrate are shown to be the main parameters that quantify the retraction, the breaking time, and the number of agglomerates. Moreover, it is found that mild surface energy anisotropy with an energy minimum in the horizontal plane postpones the mass detachment. Simple models of the γ-plots for the surface energy illustrate the influence of cusp points on the retraction profiles. Finally, the smooth and facetted experimental surfaces, that are observed in the Si/SiO_2 system after 900 °C annealing under H_2, are explained by a quite small anisotropy of the γ-plot.

DOI: 10.1103/PhysRevB.73.115427 PACS number(s): 68.35.−p, 68.55.Jk, 68.37.−d, 81.16.Rf

I. INTRODUCTION

Thin solid films are basic building blocks in microelectronics and optoelectronics. However, due to the shrinking of the layer thickness imposed by technology requirements, the surface to volume ratio is drastically increased and this leads to capillarity instabilities. To ensure device reliability, these morphological instabilities of stacked layers must be controlled during the elaboration process to avoid an agglomeration phenomenon that occurs well below the melting temperature. For example, it has been observed that during a classical thermal annealing at 850 °C (~2/3 of the Si melting temperature), a 10.5 nm silicon on insulator (SOI) film can be fully agglomerated in a few minutes.[1] It has been reported that the thinner the Si film is, the quicker the agglomeration occurs.[1] More generally, the thermal stability of silicon[1–10] and metals[11–13] on amorphous substrates has been intensively studied.

In order to prevent the morphological evolution of the thin films, the influence of the main physical ingredients must be identified. It is well known that an unstrained nearly plane infinite solid surface flattens due to capillarity effects,[14] whereas the boundaries of thin patterns must be considered as destabilizing zones because they do not usually minimize the surface energy.[15] At a temperature between half and two thirds of the melting temperature of a crystalline material, it is generally assumed that surface diffusion dominates the other transport processes of matter, namely viscous flow, evaporation/condensation, and volume diffusion.[14,16,17] Wong has studied the surface morphology evolution driven by surface diffusion in the case of semi-infinite, isotropic, and unstrained film using a numerical approach.[15,18]

For typical annealing temperatures in the 650 °C–900 °C range, it has been shown that specific directions are favored during the retraction of a Si film from a SiO_2 substrate.[3–6] This indicates that the anisotropy of surface energy and/or diffusion needs to be taken into account. The surface diffusion anisotropy has not been seen to be sensitive in two dimensions (this paper's framework), contrary to the surface energy anisotropy (see hereafter). Moreover, a 1 nm Si film (not voluntarily strained) on SiO_2 has a residual biaxial stress of less than 100 MPa grazing incidence x-ray diffraction (GIXRD) measurements have been performed to confirm this point). Considering the Grinfeld-Azaro-Tiller instability, this stress state is not destabilizing for continuous films thinner than 15 nm.[19] In consequence, this paper focuses on the effect of the anisotropy of the surface energy neglecting the strain energy. This paper will address the general problem of the two-dimensional (2D) retraction of a finite anisotropic film from a rigid substrate. An interesting case to study is an initial sharp step profile as shown in Fig. 1(a). This profile, representing for example a patterned SOI substrate, exhibits two singular points: the upper corner and the contact point with the substrate. It is generally calculated[15,18] and confirmed by our experiments (see hereafter Fig. 11) that the film retracts with a thickened edge followed by a valley as shown in Fig. 1(b). The film may pinch off after a breakup time called t_c. Phenomenology and dynamics differ with regard to the aspect ratio of the initial patterned film and the contact angle. In this paper, a discrete calculation of the surface chemical potential is developed to take large curvature morphologies and mass conservation into account. This will be applied to the solid-state dewetting phenomenon to understand the influences of the contact angle and aspect ratio. This approach can also be used to simulate other physical problems such as hole growth or thermal grooving. It allows taking the anisotropy of the physical properties that significantly alter the dynamics of the shape evolution[20] into account, as well as the final equilibrium shape known as the Wulff's construction.[21]

The following section presents the physical basis of the problem. The numerical method used to solve the evolution equations is described in Sec. III, applied to the dewetting of a finite solid film with different aspect ratios and compared

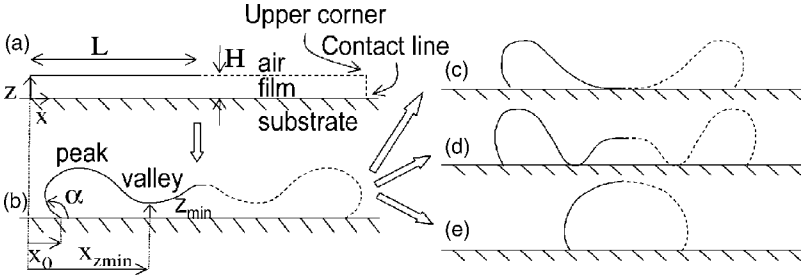

FIG. 1. Schematics of the dewetting of a thin film of thickness H and length $2L$. Only half of the film is drawn due to symmetry consideration. The contact angle between the film and the substrate is described by α. The initial edge (a) retracts (see x_0) and the profile forms a peak followed by a valley (b). The film evolves until peeling off in two (c) or three (d) agglomerates, or it rearranges in single agglomerate (e).

to experimental profiles in Sec. IV. Different physical assumptions will be considered: mass retraction with isotropic surface energy (Sec. IV A) as well as mild and severe anisotropy (Sec. IV B). Finally, discussion and general conclusions are presented in Sec. V.

II. PHYSICAL MODEL

In this paper, surface diffusion will be described by the surface chemical potential μ defined as the derivative of the Gibbs free energy G with respect to the number of atoms at constant temperature T and stress $\mu=(\partial G/\partial N)_{T,stress}$.[22] It is supposed that the system temperature is homogeneous and, as long as the strain effect is neglected, the derivative of G with respect to N can be seen as an infinitesimal increment ∂G over the infinitesimal increment of volume ∂V: $\mu=\Omega_0(\delta G/\delta V)$ where Ω_0 is the atomic volume.

In the case of unstrained films and by neglecting the surface stress, the Gibbs energy variation can be taken as the variation of the integral of the surface energy γ over the surface: $\delta G=\delta\int_{\text{surface}}\gamma dS$. Considering an infinitesimal protrusion on a smoothly curved surface, Herring[22] demonstrates that the corresponding increment in Gibbs energy is equal to $(\gamma+\gamma')\kappa\delta V$, where κ is the surface curvature and the prime denotes the derivation over the angle θ formed between the tangent to the surface and a reference plane. This leads to the following one dimensional (1D) expression: $\mu=\Omega_0(\gamma+\gamma')\kappa$. This latter potential value is only valid at low curvature and then cannot be applied to a facetted surface. So, the derivative form of μ will be preferred in the following.

According to the Nernst-Einstein equation,[17] the surface potential gradient will produce a drift of surface atoms with a flux

$$\vec{J}=-\left(\frac{D_s\nu}{k_BT}\right)\cdot\vec{\nabla}_S\mu, \tag{1}$$

where $\vec{\nabla}_S$ is the surface gradient operator, D_s is the surface diffusion coefficient, ν is the number of atoms per unit area, and k_BT is the thermal energy. For an isotropic surface energy and an infinite film,[14] the above equation shows that the surface tends to flatten (atoms flow from high to low curvature areas).

The infinitesimal increment of matter δN is expressed by the matter conservation law

$$\delta N=\left(-\int\int_S \text{div}(\vec{J})\cdot\vec{dS}\right)\cdot\delta t \tag{2}$$

Assuming a constant atomic volume Ω_0, the volume increment δV is simply related to δN by: $\delta V=\Omega_0\times\delta N$.

In order to obtain dimensionless equations, the material dependent parameters and the temperature are included in a constant B

$$B=\frac{D_s\gamma_0\nu\Omega_0^2}{k_BT}, \tag{3}$$

where γ_0 is a surface energy reference (detailed in Sec. IV B). The initial film thickness H constitutes a natural length scale and time is made dimensionless by the H^4/B factor. As the dimensionless space variable is only a function of H, the profile shape will only depend on the geometry and not on the material properties included in B. This latter parameter will steer the time evolution.

The evolution of the initial profile will be determined by Eqs. (1) and (2) (a fourth-order differential equation) and by four boundary conditions given in the following section.

III. NUMERICAL METHOD

As shown in Fig. 2, three consecutive points M_{i-1}, M_i, and M_{i+1} of the 1D surface are considered. At each point, the numerical method developed in this paper consists of a sequence of three steps that will be detailed hereafter: (i) calculation of the surface potentials μ_i from the differential definition; (ii) calculation of local increments of matter δN_i from Eq. (2); and (iii) the displacement of the points.

(i) The chemical potential μ_i is calculated considering an infinitesimal displacement $\delta\eta_i$ of M_i perpendicular to (M_{i-1},M_{i+1})

$$\mu_i=\mu^0+\lim_{\delta\eta_i\to 0}\left(\frac{\delta G_i(\delta\eta_i)}{\delta V_i(\delta\eta_i)}\right), \tag{4}$$

where μ^0 is a constant which can be set to zero without loss of generality. Considering the notations of Fig. 2 for the surface energies γ_i and the segment lengths b_i, l_i, $h_{o,i}$, this equation yields

$$\mu_i=\mu^0+\frac{2}{b_{1,i}+b_{2,i}}\times\left\{h_{0,i}\left(\frac{\gamma_{i-1}}{\ell_{i-1}}+\frac{\gamma_i}{\ell_i}\right)+\left(\frac{b_{2,i}\gamma_i'}{\ell_i}-\frac{b_{1,i}\gamma_{i-1}'}{\ell_{i-1}}\right)\right\}. \tag{5}$$

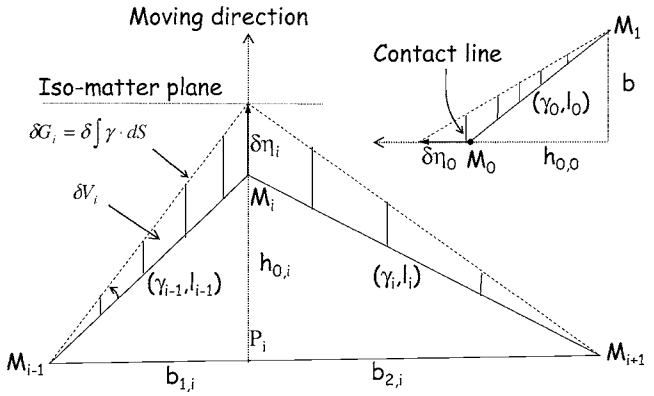

FIG. 2. Sketch for the calculation of the surface chemical potential according to Eq. (5) (see text) at the point M_i between M_{i-1} and M_{i+1}, which is not positioned at the boundary with the substrate. l_{i-1} (γ_{i-1}) and l_i (γ_i) are the length (surface energies) of the segment $[M_{i-1}M_i]$ and $[M_iM_{i+1}]$. $h_{0,i}$ is the distance between M_i and $(M_{i-1}M_{i+1})$. $b_{1,i}$ and $b_{2,i}$ are respectively the distance between M_{i-1} and M_{i+1} to P_i, the orthogonal projection of M_i on $(M_{i-1}M_{i+1})$. δV_i and δG_i are respectively the increment of volume and energy of the surface after a displacement $\delta\eta_i$ of M_i along $[P_iM_i]$. The inset shows the sketch of the calculation of the surface chemical potential at the point M_0 on the contact line.

It is worth noting that μ_i does not depend directly on the second derivative of the surface energy, but on its first derivative. However, considering an isosceles triangle (M_{i-1}, M_i, M_{i+1}) and the low curvature limit $(h_{0,i} \to 0)$, it is easy to deduce the finite difference form of the Herring formula $\mu = (\gamma + \gamma'')\kappa$.

Only half of the whole system needs to be simulated due to symmetry consideration. The chemical potential values on the axis of symmetry and at the triple point define the first two boundary conditions. The chemical potential μ_n on the axis of symmetry is calculated using Eq. (5) adding a fictive point M_{n+1}, symmetric about M_{n-1}. Since the main concern is with discontinuous films, the most important place to observe is the point on the contact line between the layer and the substrate. As shown in the inset of Fig. 2, the chemical potential μ_0 at the contact line is calculated following Eq. (4) where $\delta\eta_0$ is taken along the substrate/film interface and δG_0 is the sum of the surface and interface energy contributions

$$\mu_0 = \mu^0 + \frac{2}{b} \times \left\{ h_{0,0}\frac{\gamma_0}{\ell_0} - \frac{b\gamma_0'}{\ell_0} - (\gamma_{sub} - \gamma_{sub/film}) \right\} \quad (6)$$

Furthermore, this procedure facilitates simulation of film motion with $\gamma_{sub} - \gamma_{sub/film} = \pm\gamma_0$ corresponding to null or 180° contact angles. This point is difficult to implement with other numerical methods when the contact angle is directly imposed as a boundary condition.

(ii) The flux of matter given by Eq. (1) is simply calculated by a finite-difference method along a segment between two consecutive points. For a 1D surface, the matter increment δN_i attributed to the point M_i ($i \neq 0$ and $i \neq n$) is the algebraic sum of the fluxes along the two segments ending on M_i multiplied by the time step dt. The triangle (M_{i-1}, M_i, M_{i+1}) will then grow or shrink depending on the sign of this sum. The two last boundary conditions necessary to solve the dynamic equations are given by the zero mass flux through the symmetry axis and the contact line. This ensures the mass conservation of the system. The flux going to the symmetry axis at point M_n is the sum of the two symmetric fluxes from M_{n-1} and the fictive point M_{n+1}. The flux going to the contact line at point M_0 is reduced to the flux from M_1.

(iii) Each M_i point ($i \neq 0$) is displaced by δz_i perpendicular to the base of each (M_{i-1}, M_i, M_{i+1}) triangle. Using dimensionless equations in the 2D case, the matter increment δN_i is equivalent to the surface increment, so that δz_i is the matter increment δN_i divided by the length of the base of the (M_{i-1}, M_i, M_{i+1}) triangle (called $b_{1,i}+b_{2,i}$ in Fig. 2): $\delta z_i = \delta N_i/(b_{1,i}+b_{2,i})$. The general conservation of matter has been checked during the calculation. The displacements of M_0 (resp. M_n) is forced to be parallel to the substrate (resp. to the axis of symmetry) to ensure zero mass flux.

The present numerical approach can be adapted to several different physical problems by simply changing the four boundary conditions which represent the potentials and fluxes at the boundaries of the system.

In the early part of the simulation of the film retraction, surface displacement close to the edge is quite large compared to that close to the symmetry axis. Nevertheless, at a later stage, the instability propagates towards the middle of the film. To achieve good accuracy without excess CPU time consumption, the initial mesh is tightened close to the edge and made coarse far from it. Then, during simulation, the mesh is automatically slowly adapted to follow the instability propagation. At each time step, the positions of the M_i points are shifted parallel with (M_{i-1}, M_{i+1}) towards the median of $[M_{i-1}, M_{i+1}]$ of a distance proportional to the distance between M_i and the median of $[M_{i-1}, M_{i+1}]$. A coefficient of proportionality of 0.01% has been empirically validated. This lateral movement does not change matter quantity, and the mesh becomes nearly homogeneous after ~ 2–3×10^5 time steps. This scheme stabilizes the numerical code and enables a decrease in the CPU time by about one or two decades without significant information loss. The comparison of the evolution of films simulated with n points and $2n$ points validates the numerical accuracy of this method (n ranging from 100 to 200). In the worst case, the time and position where the film pinches off differs by less than 1.5% and 0.5%, respectively. The temporal convergence was obtained by decreasing the time step dt until the breakup time t_c differed by less than 0.2% using dt and $dt/2$ time steps.

The code has been checked with three time-dependent problems described in the literature. First, an initial rectangular profile in free air converges at large times for any γ-plot (isotropic or not) to the thermodynamic equilibrium shape given by the Wulff's construction where $\int_s \gamma dS$ is minimum.[21] Second, an initially sinusoidal profile, with small amplitude compared to its period, conserves its sinusoidal shape and decreases its amplitude exponentially with time in agreement with the analytical solution $z(x,t) = A\exp[-B(2\pi/\lambda)^4 t]\sin(2\pi x/\lambda)$ [where A and λ are constant with $A \ll \lambda$, and B is given by Eq. (3)] discussed by Mullins,[14] Lançon,[23] and Cahn.[24] Third, the retraction of an isotropic semi-infinite film step on a substrate is reproduced

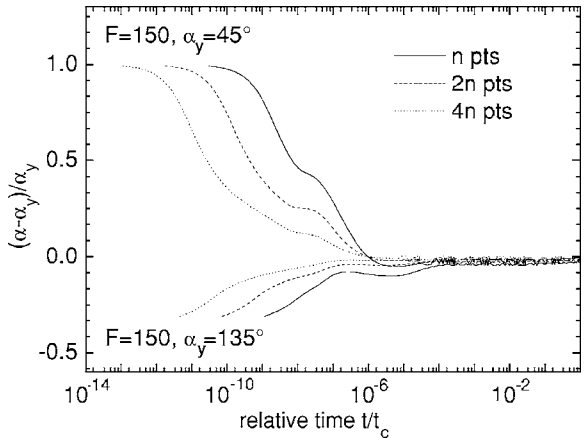

FIG. 3. Relative difference $(\alpha-\alpha y)/\alpha y$ between the contact angle α and the equilibrium contact angle α_y as a function of time normalized by the breaking up time t_c. Simulations are carried out with n, $2n$, and $4n$ points ($n=75$), an aspect ratio of $F=150$, and dimensionless adhesion energies corresponding to Young contact angle of 45° and 135°. α converges to α_y at least four decades before t_c.

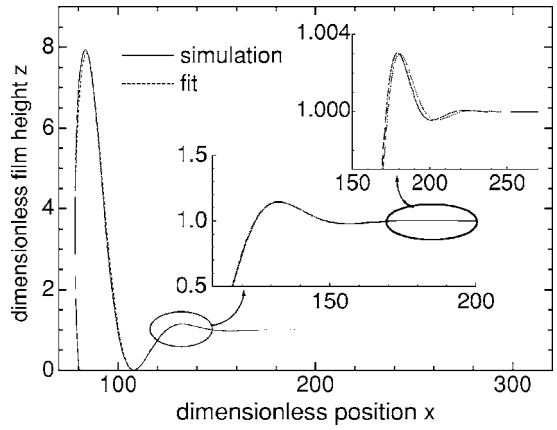

FIG. 4. Surface profile simulated for an isotropic surface energy (see Sec. IV for the numerical procedure). The initial state is shown in Fig. 1(a) with $F=L/H=500$, the equilibrium contact angle is 160°, and the time is $t=13\,000$. The insets zoom in on the second and third peaks. A fit of the profile with the function $z(x,t)=1+A(t)\exp[-kx/x_p(t)]\cos[2\pi x/x_p(t)+\varphi]$ is given with $A(13\,000)=6700$, $k=3.87$ (close to the value given by Srolovitz (Ref. 24): $2\pi/\sqrt{3}\approx 3.63$), $\varphi=1.1$ rd and $x_p=48.33$ $x_p(t)$ is found to vary as: $x_p(t)\approx 5.4t^{0.23}$.

in agreement with the results of Wong[15] for the complete range of contact angle. This point which will be detailed later, appears as a particular case of the finite film retraction developed in Sec. IV A for isotropic surface energy. More generally, the surface energy anisotropy effects (with or without cusp points) will be discussed in Sec. IV B.

IV. SIMULATION OF THIN FILM RETRACTION

A. Isotropic surface energy

As shown in Fig. 1, at the first stage of the simulation, the film profile changes at the contact point to reach the equilibrium contact angle α_y given by the Young equation: $\gamma_{sub}-\gamma_{sub/film}=\gamma_0\cos(\alpha_y)$ where γ_{sub} is the surface energy of the substrate and $\gamma_{sub/film}$ is the energy of the substrate/film interface. In the anisotropic case, γ_0 is replaced by $\gamma(\alpha_y)$ and a nontrivial solution must be calculated. Note that this equation is derived by calculating the variation of the surface free energy caused by a small displacement $\delta\eta_0$ of the triple point[26] which corresponds exactly to our numerical method for the calculation of surface potential. Figure 3 shows that the convergence of α to α_y is very fast and the local equilibrium state is reached four orders of magnitude before the breakup time t_c. It has also been checked that the equilibrium state can be achieved even more quickly with a tightened mesh, and that t_c is, to a first approximation not significantly influenced by the early nonequilibrium state close to the triple line. In consequence, we can consider that the contact angle equilibrium is quasi-instantaneous compared to general profile evolution. For the sake of simplicity, we will use the contact angle $\alpha(t\to\infty)=\alpha_y$ in the text as a system variable instead of its equivalent in energy $(\gamma_{sub}-\gamma_{sub/film})$. In Fig. 3, the variation of $\alpha-\alpha_y$ at later time $(t/t_c>10^{-4})$ corresponds to numerical noise and is mainly determined by the time step.

In the second stage, the film smoothes the sharp edge in order to reduce the surface energy in agreement with the numerical results of Wong[15] and the analytical steady state solution derived by Srolovitz and Safran in the small slope limit $(\partial z/\partial x\ll 1)$.[25] Figure 4 plots an example of the profile with a solution-like fit calculated by Srolovitz and Safran.

The first valley from the edge corresponds to the minimum film thickness and is denoted z_{min} (Fig. 1). Its evolution as a function of time for $\alpha=45°$ and for different aspect ratios $F=L/H$ is presented in Fig. 5(a) (H and L are respectively the initial film thickness and half length). At large F (more than about 500), a semi-infinite behavior is observed.[15] $z_{min}(t)$ decreases continuously with time and reaches the substrate at t_c. At this time, mass is detached from the film, and at least 3 agglomerates will be formed [Fig. 1(d)]. For smaller F, the edge coupling induced by the surface diffusion mechanism cannot be neglected and $z_{min}(t)$ oscillates around the semi-infinite case until it strongly decreases leading to the breaking point. Moreover, the total energy of the film, the retraction quantity x_0, and the position of the first minimum x_{zmin} oscillate around the semi-infinite case with amplitude increasing with time. Two or three agglomerates can be observed as in Figs. 1(c) and 1(d). If the film breaks in the middle, 2 agglomerates are formed; if not, at least 3 agglomerates are formed. It is worth noting that the breaking time can be largely brought backward and can occur a decade before the semi-infinite case. For even smaller F values ($F<100$), coalescence occurs and the film never breaks [Fig. 1(e)].

The influence of α on z_{min} is shown in Fig. 5(b) for $F=150$. The breaking time t_c is decreased with α. It indicates that the coupling between the two film edges appears later for acute angles. A limit between the regimes of weak and strong edge coupling can be drawn. To further analyze the dependence of critical breaking time t_c on both F and α, Fig.

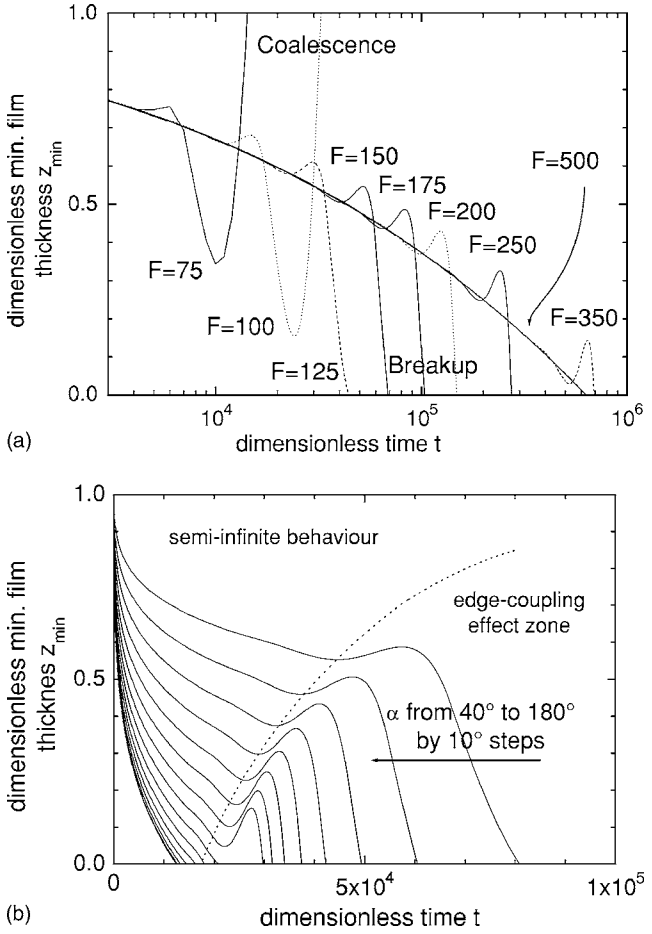

FIG. 5. Evolution of the minimum dimensionless film thickness z_{min} (see Fig. 1) vs dimensionless time t for a contact angle of 45° and for different aspect ratio F. The surface energy is considered to be isotropic. $F=500$ is close to the semi-infinite case. When z_{min} reaches 0, the film breaks up, and when z_{min} goes higher than 1, the dip is filled up and the matter rearranges in single agglomerate. $z_{min}(t)$ oscillates around the semi-infinite case with amplitude increasing with time, before the breakup or the coalescence. b) Minimum dimensionless film thickness z_{min} vs dimensionless time t for an aspect ratio $F=150$ and for different contact angle α. Edge-coupling effect and breakup time appear earlier with an increase of the contact angle.

6 plots $\ln(t_c)$ as a function of $\ln[1/\sin(\alpha/2)]$for different F values. Two clear regimes can be identified on this figure. At large F and α, t_c is independent of F and increases as α decreases. In this region, no edge coupling effect is observed and the behavior is close to the semi-infinite film case. A Taylor development at small α of the fit of the linear portion in Fig. 6 (see figure caption) gives: $t_c=211\times10^3\times\alpha^{-4}$ in agreement with Wong.[15] When decreasing F and/or α, t_c follows a law depending on both F and α that can be empirically fitted by $\ln(t_c)=C_1/\sin(\alpha/2)+C_2$ where where C_1 and C_2 linearly depend on $\ln(F)$ and are given in the caption of Fig. 6.

The number of agglomerates (1, 2, 3, and more) is given in Fig. 7 in the $[\sin(\alpha/2)^{-1},F]$ coordinates. In this representation, the domain boundaries correspond to straight lines indicating the increase of the areas with F and $\sin(\alpha/2)^{-1}$.

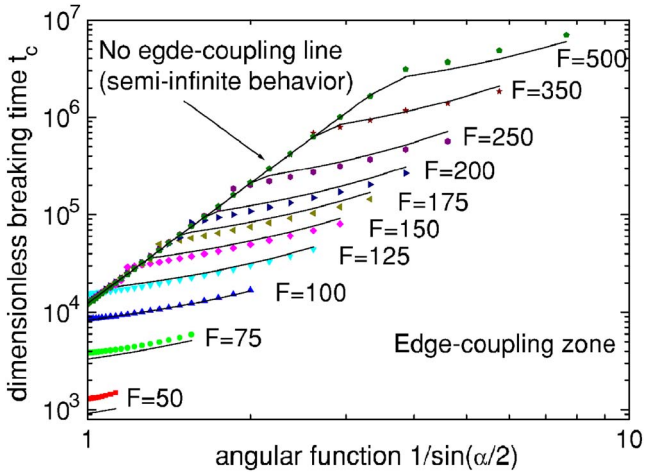

FIG. 6. (Color online) Logarithm of the critical breakup time t_c:$\ln(tc)$ as the function of $\ln[1/\sin(\alpha/2)]$ (α: contact angle) for different aspect ratio F. The points correspond to numerical simulations for an isotropic surface energy, and the lines to empirical adjustments. Two regimes can be identified. The first one is the region where the edge-coupling effect is negligible. $t_c(F,\alpha)$ depends only on F, and can be fitted by: $\ln(t_c)=4.092\ln[1/\sin(\alpha/2)]+9.4225$. In the second one, the edge coupling cannot be neglected and t_c is depending both on α and F. t_c is relatively well fitted by the general law: $\ln(t_c)=C_1/\sin(\alpha/2)+C_2$, where $C_1=-0.328\ln(F)+2.23$ and $C_2=3.42\ln(F)-7.39$.

The fits of the boundaries between the different regions given in the caption of Fig. 7, allows prediction of the fragmentation of the film of a given material only defined by its adhesion energy (i.e., α). The above phenomenology of the film retraction will now be considered taking into account the anisotropy in the surface energy.

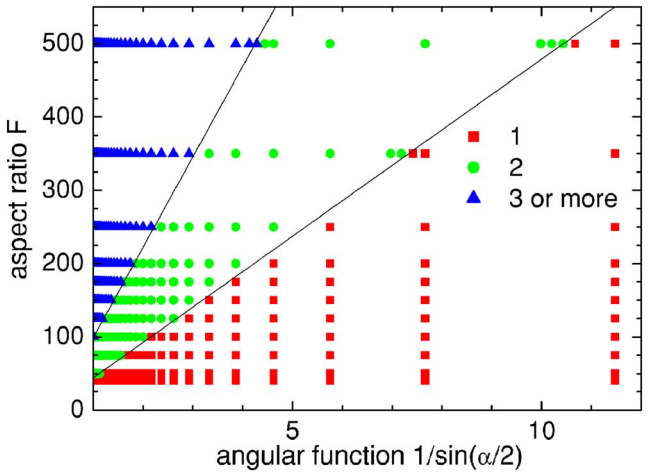

FIG. 7. (Color online) Number of agglomerates calculated with an isotropic surface energy vs $1/\sin(\alpha/2)$ (α is the contact angle) and aspect ratio F. The points correspond to the numerical simulations. The dashed lines show the boundaries for the formation of 1, 2, and 3 or more agglomerates. They can be fitted by $F=48.3/\sin(\alpha/2)-4.33$ for 1–2 agglomerates and $F=123.4/\sin(\alpha/2)-24.6$ for 2–3 and more agglomerates.

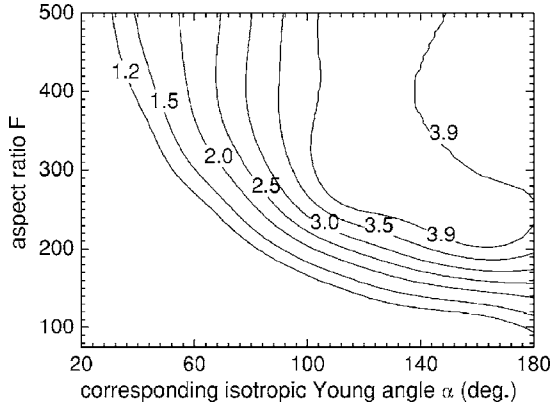

FIG. 8. Ratio of anisotropic to isotropic breaking time ($t_{c,aniso}/t_{c,iso}$) vs the corresponding isotropic Young angle α and the aspect ratio F. The anisotropic surface energy follows Eq. (7) with $\xi=0.013\,32$ and $\theta=\pi/8$. For large F and α, t_c can be several times higher in the anisotropic case than in the isotropic one.

B. Anisotropic surface energy

Surface anisotropy has been considered in two ways depending on the surface stiffness parameter $\Sigma(\theta)=\gamma+\partial^2\gamma/\partial^2\theta$ and on the existence of cusp points in the γ-plot curve. The anisotropy is called mild for strictly positive $\Sigma(\theta)$ and severe in the other case.[20] For mild anisotropy, all plane orientations are stable and no faceting is expected.[20] For severe anisotropy, missing angles exist in the Wulff's construction. Cusp points in the γ-plot curve have been introduced to fit the experimental results where spontaneous faceting occurs. For consistency, the anisotropic and isotropic cases will always be compared with the same nondimensional adhesion energy $\Delta W^*=(\gamma_{sub}-\gamma_{sub/film})/\gamma_0-1$ and we will consider the corresponding isotropic Young angle: $\alpha_y=\cos^{-1}(\Delta W^*+1)$.

1. γ-plot without a cusp point

For the sake of simplicity, an eightfold normalized γ-plot is assumed

$$\frac{\gamma(\theta)}{\gamma_0}=1+\xi\cos[8(\theta-\theta_0)]. \tag{7}$$

$\theta=0$ corresponds to the reference plane (parallel to the substrate), γ_0 is the average of the surface energy on θ, and ξ, θ_0 are two adjustable constants. This function is compatible with cubic symmetry,[20,27] and yields to the surface stiffness: $\Sigma(\theta)=1-63\xi\cos[8(\theta-\theta_0)]$. So, $\xi<1/63$ leads to a mild anisotropy and $\xi\geqslant 1/63$ to a severe one. The experimental measurements of Bermont[28] for silicon at 1323 K give a weak anisotropy around $\gamma_{max}/\gamma_{min}-\langle\gamma(\theta)\rangle=0.027$ corresponding to a mild anisotropy with $\xi=0.013\,32$ [where $\langle\gamma(\theta)\rangle$ is the average of the surface energy on θ]. θ_0 is set to $\pi/8$ to fix an energy minimum at the (O,x,y) plane parallel to the substrate. Film motion has been simulated with these ξ and θ_0 values and for different α (0° to 180°) and F (40 to 500). Figure 8 shows the ratio of anisotropic to isotropic breaking time ($t_{c,aniso}/t_{c,iso}$) as a function of (α,F). For large α and F, the critical breakup time t_c is several times higher than in isotropic case, and $t_{c,aniso}/t_{c,iso}$ increases with α and F. On the contrary, when the coupling effect cannot be neglected, $t_{c,aniso}$ does not vary more than 20% compared to $t_{c,iso}$.The number of agglomerates vs. α and F for this anisotropic surface energy is presented in Fig. 9. The boundaries between the numbers of agglomerates (solid lines) are shifted to large F and α compared to the isotropic case (dashed lines). To conclude with a smooth eightfold γ-plot where the plane parallel to the substrate has a minimum in energy, the film gains in stability regarding to t_c and to the number of agglomerates. Simulations with $\xi>1/63$ (not shown here) have also shown that this gain can be enlarged with severe eightfold γ-plot, and that t_c is postponed even further with an increase of ξ.

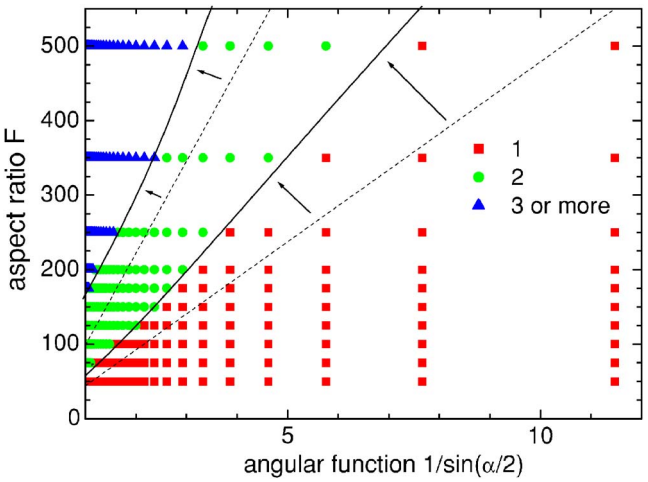

FIG. 9. (Color online) Number of agglomerates calculated with an anisotropic surface energy (defined by Eq. (7) with $\xi=0.013\,32$ and $\theta_0=\pi/8$) as a function of $1/\sin(\alpha/2)$ (α is the corresponding isotropic Young angle) and aspect ratio F. The points correspond to the numerical simulations. The boundaries between the numbers of agglomerates (solid lines) are shifted compared to the isotropic surface energy calculations (dashed lines taken from Fig. 7).

The dependence of t_c on θ_0 with the same eightfold γ-plot has been checked with $\xi=0.013\,32$ and $\theta_0=0$, $\pi/16$, $\pi/8$, and $3\pi/16$ corresponding to a γ-plot rotation. For $\theta_0=0$ and $\pi/8$, the plane parallel to the substrate is a maximum and a minimum in surface energy, respectively. In the two other cases, the plane (O,x,y) is neither a minimum nor a maximum. The surface profiles are reported in Fig. 10 for $t=3000$, $\alpha=135°$, and $F=250$ (i.e., without edge coupling). Table I gives the relative position of the first valley compared to the isotropic configuration. It is observed that for $\theta_0=\pi/8$ (0), the first valley is shallower (deeper) than the isotropic case. For $\theta_0=\pi/16$ ($3\pi/16$), the position of the minimum thickness moves away (gets closer) from the edge than the isotropic case. This can be explained as follows. For the γ-plot of Eq. (7), a minimum surface energy occurring at (O,x,y) for $\theta_0=\pi/8$ corresponds to a maximum surface stiffness that locally favors a low curvature to maintain a low gradient of μ. The opposite behavior is obtained for $\theta_0=0$. For $\theta_0=\pi/16$ and $3\pi/16$, the (O,x,y) plane has the same energy as in the isotropic case, and z_{min} is similar. But, the positions of the valleys differ along x. For $\theta_0=\pi/16$, the

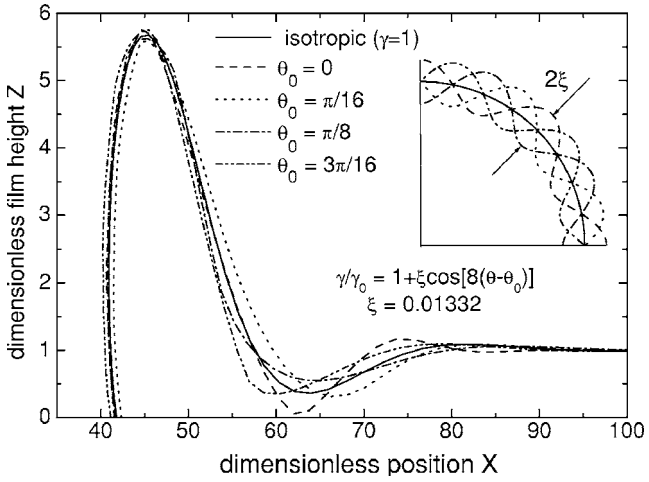

FIG. 10. Surface profiles corresponding to a film retraction with an anisotropic surface energy without a cusp point. The eightfold γ-plots and equation are shown in the inset. Four orientations θ_0 of the minimum in surface energy are drawn and discussed in the text. The corresponding isotropic Young angle α is 135° and dimensionless time is 3000. The film aspect ratio is $F=250$, i.e., long enough to avoid the edge-coupling effect. The initial sharp corner [see Fig. 1(a)] was at the abscissa $x=0$.

plane with the orientation $\theta=-\pi/16$ is more stable and the valley moves away from the first peak to enlarge this plane orientation. Inversely, for $\theta_0=3\pi/16$, the plane with the orientation $\theta=\pi/16$ is more stable and the valley gets closer to the first peak to enlarge this plane. These interpretations stay valid for a large range of α (confirmed from 45° to 165°) and larger ξ (in the mild and severe cases).

2. γ-plot with cusp points: The case of Si(001) films

It has been seen that with a γ-plot without a cusp point, severe or not, the geometry close to the first valley can be very different whereas the retraction quantity x_0 of the contact line is roughly the same (see Fig. 10). Moreover, in every case, a dip below the initial thickness follows the first peak. This is in agreement with the retraction of SOI at 950 °C as seen in Fig. 11. This atomic force microscopy (AFM) picture represents the three-dimensional (3D) profile

TABLE I. z_{min} and x_{zmin} (see Fig. 1) carried out from the anisotropic cases of Fig. 10, for different θ_0 compared to the isotropic case. When the surface energy of the $(0,x,y)$ plane is a minimum ($\theta_0=\pi/8$), the hollow is shallower, and inversely for $\theta_0=0$. When $\theta_0=\pi/16$, the plane disoriented by $-\pi/16$ from $(0,x,y)$ is a minimum of energy and the peak tends to develop this plane, so the valley moves away from the first peak compared to the isotropic case, and inversely for $\theta_0=3\pi/16$.

	z_{min}	x_{zmin}
$\theta_0=0$	$<$	$\approx$
$\theta_0=\pi/16$	$\approx$	$>$
$\theta_0=\pi/8$	$>$	$\approx$
$\theta_0=3\pi/16$	$\approx$	$<$

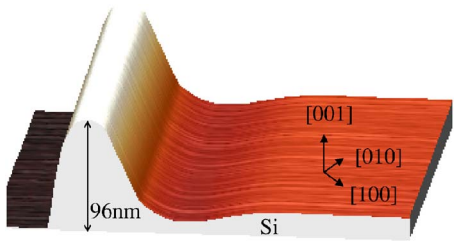

FIG. 11. (Color online) 1.5 μm $\times$ 1.5 μm AFM image (tapping mode) of the edge retraction of a film of Si on SiO_2 after a 30 mn annealing at 950 °C (initial thickness 13.8 nm). The first peak is 96 nm high and is followed by a dip. This profile is similar to the retraction simulations with an isotropic surface energy model.

of a 13.8 nm initial film thickness of Si on SiO_2 close to the initial sharp corner, after 30 min annealing at 950 °C under H_2 atmosphere. This experimental profile is close to the prediction of the diffusion motion model presented so far. However, with similar experimental conditions (13.0 nm film thickness, 2 min annealing at 900 °C under H_2 atmosphere), a facetted profile can also be observed as illustrated in Fig. 12. A matter front is observed with well-defined facets and without a dip in the film. This image has been analyzed by use of a polar plot revealing the {113} planes on the four sides of the top of the matter front whereas the plane $(\bar{1}\bar{1}1)$ is developed close to the contact line. Note that the top of the peak seems not to be perfectly flat (see Fig. 12). The difference between the experimental results presented in Figs. 11 and 12 might be explained by the temperature difference. Minima of the experimental γ-plot are probably not very sharp.[28,29] So, the γ-plot must be very sensitive to wafer contamination or structural defects. Actually, a fraction of carbon monolayer on silicium can drastically modify the surface energy anisotropy[30] and can explain the highly facetted profile in Fig. 12.

To fit the experimental dewetting profile shown in Fig. 12, the γ-plot needs to be modified to include cusp points at the

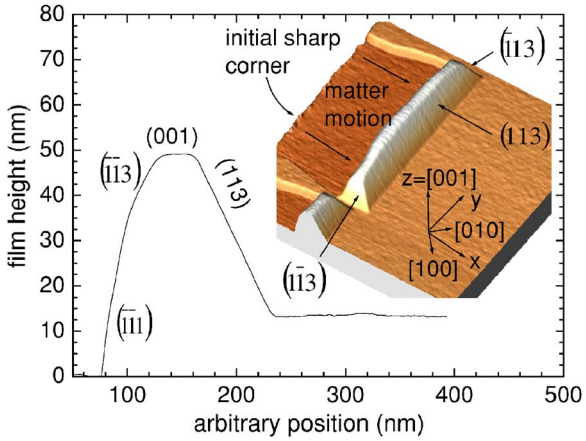

FIG. 12. (Color online) Image: 1 μm $\times$ 1 μm AFM image (tapping mode) of the Si on SiO_2 retraction after a 2 min annealing at 900 °C (the initial film thickness is 13.0 nm). The peak is facetted and reaches 52 nm high. No dip appears behind the (113) plane. Curve: Profile along $(0,x)$. It is similar to the retraction simulations with an anisotropic surface energy model.

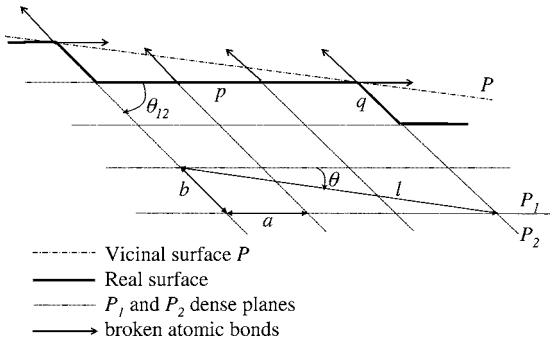

FIG. 13. Schematics of 2D network of atoms placed at the intersection of two dense planes P_1 and P_2. The disorientation angle between P_1 and P_2 is θ_{12}. The distance between the P_1 planes is a and between the P_2 planes is b. The disorientation angle of the vicinal surface is θ from the reference planes P_1. The terrace and step length are respectively p and q. The distance between 2 consecutive steps is l.

angles corresponding to the experimental minimum in energy, namely the {001}, {113}, {111}, and {110} planes (the $(1\bar{1}0)$ plane cannot be probed on the AFM image, but {110} planes have been observed on single agglomerates). A semiempirical analytic γ-plot has been developed for this purpose within a simple bond-breaking model where surface passivation, reconstruction, relaxation, and step interactions are not considered. This can be described by considering two dense planes P_1, P_2 of surface energies γ_{P_1}, γ_{P_2} separated by an angle θ_{12}, and a vicinal plane P with a disorientation angle θ from $P_1(0 \leqslant \theta \leqslant \theta_{12})$ (see Fig. 13). Let l be the distance between 2 steps, x the length of the terraces, y the step length, a the distance between 2 atoms on P_1, and b the distance between two atoms on P_2, as schematized in Fig. 13. The numbers of atomic bonds broken on P_1 along the length p and on P_2 along the length q are, respectively

$$\frac{p}{a} = \frac{l}{a}\left(\cos(\theta) - \frac{\sin(\theta)}{\tan(\theta_{12})}\right) \text{ and } \frac{q}{b} = \frac{l\sin(\theta)}{b\sin(\theta_{12})}. \quad (8)$$

The energy of the P plane of length l is given by

$$\gamma(\theta)l = \gamma_{P1}p + \gamma_{P2}q. \quad (9)$$

It gives the expression of the surface energy per unit length of a plane with disorientation $\theta \in [0, \theta_{12}]$

$$\gamma(\theta) = \gamma_{P1}\left(\cos(\theta) - \frac{\sin(\theta)}{\tan(\theta_{12})}\right) + \gamma_{P2}\frac{\sin(\theta)}{\sin(\theta_{12})}. \quad (10)$$

For that particular γ-plot, only dense plane orientations appear on the Wulff's construction. It can be demonstrated that this type of γ-plot is formed of portions of circles going through the origin. To the first order, this γ-plot is equivalent to the one generally developed for a vicinal surface with a step-free energy β given by (where h is the step height)[29]

$$\frac{\beta}{h} = \frac{\gamma_{P2}}{\sin(\theta_{12})} - \frac{\gamma_{P1}}{\tan(\theta_{12})}. \quad (11)$$

The γ-plot used to simulate the experimental dewetting of (001) silicon on SiO_2 (see the inset of Fig. 14) is defined by

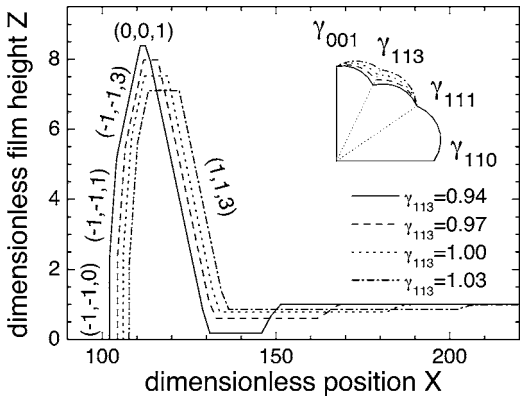

FIG. 14. Surface profiles corresponding to a film retraction with an anisotropic surface energy with cusp point. The inset shows the γ-plot with a 12-fold symmetry corresponding to the $\lfloor 1\bar{1}0 \rfloor$ zone and to the {001}, {113}, {111}, and {110} dense planes. $\gamma(\theta)$ is given by Eq. (10) between these dense plane orientations. γ_{113} is varied from 0.94 to 1.03 and the other dense plane energies are fixed to 1.00. Note that the dense plane extension on this profile directly depends on the surface energy ratio.

the $\lfloor 1\bar{1}0 \rfloor$ zone with cusp points corresponding to the dense planes {001}, {113}, {111}, and {110} joined by a curve defined by Eq. (10). This γ-plot results from a very simple model (cut valence bonds model) but has the advantages that the minima can be adjusted to be realistic and the analytic form is suitable to simulate the dewetting. Here, the reference surface energy is γ_{001} [noted γ_0 in Eq. (3)]. To simplify the writing, it was decided to use dimensionless energy and to fix $\gamma_{001} = \gamma_{110} = \gamma_{111} = 1.00$ and to vary γ_{113}. It is worth noting that the profile time evolution can be simulated for null surface stiffness for every orientation whereas it cannot be done using the potential $\mu = (\gamma + \gamma')\kappa$. Figure 14 shows that the film only exhibits dense plane orientations for γ_{113} in the $[0.94, 1.03]$ range. This is in agreement with the experimental profile given in Fig. 12. The dense planes observed in the simulation depend on the surface energy ratio and can be directly compared to the Wulff's construction. From the usual Wulff's construction, it can be shown that the four dense plane families are present in the equilibrium shape for $\gamma_{c1} < \gamma_{113} < \gamma_{c2}$ with

$$\gamma_{c1} = 3/\sqrt{11} \approx 0.9045, \quad (12)$$

$$\gamma_{c2} = \frac{\cos\left(\frac{\pi}{4} + \frac{1}{2}\arccos(\sqrt{2/3}) - \arccos(\sqrt{2/11})\right)}{\cos\left(\frac{\pi}{4} - \frac{1}{2}\arccos(\sqrt{2/3})\right)} \approx 1.125. \quad (13)$$

Below γ_{c1}, the planes {001} are unstable and above γ_{c2} the planes {113} do not appear in the Wulff's construction anymore. In Fig. 14, all four dense planes are developed for γ_{113} in the $[0.94, 1.03]$ range, in agreement with the stability domains. The relative facet extensions directly depend on the ratio of the surface energy of the dense planes. For example,

as γ_{113} increases, the (001) plane becomes larger in the Wulff's construction and appears larger on the top of the peak during dewetting. Moreover, the dip can be drastically favored or almost vanished depending on γ_{113}. As γ_{113} increases, the dip is shallower and larger, and the pinch off is postponed. A small variation of γ_{113} yields large modification of the breakup time and phenomenology. For $\gamma_{113}=0.94$, the breakup time is comparable to the isotropic case. For $\gamma_{113}\geqslant 0.97$, it is more than fifteen times larger than the isotropic case whereas for $\gamma_{113}=0.905$, it is more than sixty times lower. In the range $\gamma_{113}\in[\gamma_{c1},1.00]$, the breakup time varies over three orders of magnitude. Even for $\gamma_{113}>\gamma_{c2}$, a very shallow dip is still observed but the (111) plane is developed on the right of the peak instead of (113). For $\gamma_{113}\geqslant 1.10$, $\alpha=90°$, and $F=500$, the film does not breakup and rearranges itself in a single agglomerate. For $\gamma_{113}<\gamma_{c1}$, the peak does not exhibit a (001) plane anymore which is in agreement with stability domains, and the rest of the film develops microfacets with $(\bar{1}\bar{1}3)$ and (113) planes. For different α, the phenomenology and the breaking time are also drastically modified by a very small variation of γ_{113}. In consequence, an accurate description of the γ-plot features is needed to predict the facet morphologies. This study also indicates that surface tension anisotropy can favor the film stability from the pinch off point of view. However, the film retraction x_0 is comparable (within 20%) to the isotropic case (see Figs. 10 and 14). Indeed, the value and speed of retraction seem to be mainly governed by the contact line equilibrium, and not by anisotropy effects.

V. DISCUSSION AND CONCLUSION

A numerical method for the calculation of surface chemical potential has been developed that goes beyond the usual surface potential developed by Herring[22] which is limited to small curvature and cannot be applied to a severe anisotropy where faceting is expected. This method accommodates every anisotropic feature of the surface energy (or diffusion) and can be applied to a large number of physical problems such as hole opening, and thermal grooving as well as to nonuniform substrate interfaces (nonplanar geometry and/or nonconstant interface energy). The surface energy is described by a so called γ-plot where cusp points may occur. In this paper, the retraction of finite thin films defined by their aspect ratio has been analyzed considering only the surface diffusion mechanism. The contact line between the film and the substrate is defined by its energy, and the contact angle results from local equilibrium conditions. This is a natural result from the simulation and no numerical artifact constrain the simulation in any way. For every γ-plot, the film is stabilized in its equilibrium shape given by the Wulff's construction or by the analytic procedure given by Khare.[31]

The surface diffusion mechanism produces a minimum of the surface thickness below its initial value. As this minimum deepens, the film may break up and mass shedding may occur. During the diffusion motion of a finite film, two regimes can be clearly identified. At the beginning, the behavior of the film profile is similar to the semi-infinite geometry. Then, edge-coupling effects due to surface diffusion may be observed if the film is short enough. The aspect ratio as well as the energy of the contact line largely influences the breaking time and the phenomenology. An empirical law is proposed, predicting the fragmentation of the film defined only by these two parameters.

Experimental measurements have shown that annealing of different thin silicon patterns on amorphous silicon oxide within similar experimental conditions (thermal annealing from 900 °C to 950 °C under H_2 atmosphere) can lead to a smooth or facetted dewetting profile. The experimental facetted profiles have been fitted qualitatively by a γ-plot with cusp points and small anisotropy. The simulated and experimental profiles of Figs. 14 and 12 are in qualitative good agreement for a γ-plot following Eq. (10) and plane energies set around 1.00. For a slightly modified γ-plot, the phenomenology and the breaking time can be very different. For example, changing the surface energy at a cusp point by less than 7% can introduce a variation of the breaking time over three orders of magnitude. So, to be able to use this to predict film behavior, a very high accuracy of the γ-plot description is needed. Nevertheless, for a mildly anisotropic γ-plot with γ_{001} being a minimum, the pinch off is postponed. It can even be annihilated with γ-plots having cusp points. Therefore, from the mass detachment point of view, the stability domain can be extended thanks to surface energy anisotropy. At any given adhesion energy, our simulations show that the retraction quantity x_0 slightly depends on the γ-plot. The contact line retraction speed is not affected by the surface energy anisotropy which mainly affects the pinch off phenomenology. It appears from this study that the best way to decrease the retraction speed of the film is to increase the adhesion energy. The anisotropy of surface diffusion coefficients has not been discussed in this paper, and it could be interesting in future work to study the interplay between the faceting imposed by the surface energy and the surface diffusion coefficient anisotropies. Elastic energy could also be taken into account to simulate strained films that are currently used in microelectronics. Finally, 3D simulations could be performed with the same numerical method (including anisotropy and/or strain effects) to get better understanding of the highly symmetric experimental patterns obtained during solid-state thin film retraction.[6]

ACKNOWLEDGMENTS

We wish to acknowledge O. Cueto, D. Jamet, and B. Mathieu for advice in numerical computation. We are grateful to F. Lançon and J. Villain for many useful scientific discussions. We thank Y. Campidelli and Y. Bogumilowicz for technical assistance with the AFM instrumentation. Our gratitude is also extended to J-M. Hartmann for the time spent supporting the annealing experiments.

*Corresponding author. Electronic address: erwan.dornel@cea.fr

[1] C. Jahan, O. Faynot, L. Tosti, and J. M. Hartmann, J. Cryst. Growth **280**, 530 (2005).
[2] Y. Ono, M. Nagase, M. Tabe, and Y. Takahashi, Jpn. J. Appl. Phys., Part 1 **34**, 1728 (1995).
[3] R. Nuryadi, Y. Ishikawa, and M. Tabe, Appl. Surf. Sci. **159-160**, 121 (2000).
[4] R. Nuryadi and Y. Ishikawa, J. Vac. Sci. Technol. B **20**, 167 (2002).
[5] Y. Ishikawa, M. Kumezawa, R. Nuryadi, and M. Tabe, Appl. Surf. Sci. **190**, 11 (2002).
[6] Y. Ishikawa, Y. Imai, H. Ikeda, and M. Tabe, Appl. Phys. Lett. **83**, 3162 (2003).
[7] Y. Wakayama, T. Tagami, and S. Tanaka, J. Appl. Phys. **85**, 8493 (1999).
[8] B. Legrand, V. Agache, J. P. Nys, V. Senez, and D. Stiévenard, Appl. Phys. Lett. **76**, 3271 (2000).
[9] B. Legrand, V. Agache, T. Mélin, J. P. Nys, V. Senez, and D. Stiévenard, J. Appl. Phys. **91**, 106 (2002).
[10] M. Czubanowski, C. Tegenkamp, W. Ernst, and H. Pfnür, Appl. Phys. Lett. **84**, 350 (2004).
[11] C. M. Kennefick and R. Raj, Acta Metall. **37**, 2947 (1989).
[12] E. Jiran and C. V. Thompson, J. Electron. Mater. **19**, 1153 (1990).
[13] E. Jiran and C. V. Thompson, Thin Solid Films **208**, 23 (1992).
[14] W. W. Mullins, J. Appl. Phys. **30**, 77 (1959).
[15] H. Wong, P. W. Voorhees, M. J. Miksis, and S. H. Davis, Acta Mater. **48**, 1719 (2000).
[16] C. Herring, J. Appl. Phys. **21**, 301 (1950).
[17] W. W. Mullins, J. Appl. Phys. **28**, 333 (1957).
[18] H. Wong, M. J. Miksis, P. W. Voorhees, and S. H. Davis, Acta Mater. **45**, 2477 (1997).
[19] B. J. Spencer, P. W. Voorhees, and S. H. Davis, J. Appl. Phys. **73**, 4955 (1993).
[20] W. Zhang and I. Gladwell, Comput. Mater. Sci. **27**, 461 (2003).
[21] G. Wulff, Z. Kristallogr. **34**, 449 (1901).
[22] C. Herring, *Physics of Powder Metallurgy*, edited by Walter E. Kingston (McGraw-Hill, New York, 1951).
[23] F. Lançon and J. Villain, in *Kinetics of Ordering and Growth at Surfaces*, edited by M. G. Lagally (Plenum Press, New York, 1990).
[24] J. W. Cahn and J. E. Taylor, Acta Metall. Mater. **42**, 1045 (1994).
[25] D. J. Srolovitz and S. A. Safran, J. Appl. Phys. **60**, 255 (1986).
[26] P. Roura and J. Fort, J. Colloid Interface Sci. **272**, 420 (2004).
[27] G. B. McFadden, S. R. Coriell, and R. F. Sekerka, Acta Mater. **48**, 3177 (2000).
[28] J. M. Bermont, J. J. Métois, X. Egéa, and F. Floret, Surf. Sci. **330**, 48 (1995).
[29] J. M. Bermont, J. J. Métois, J. C. Heyraux, and F. Floret, Surf. Sci. **416**, 430 (1998).
[30] Private discussion with J. J. Métois and A. Saul.
[31] S. V. Khare, S. Kodambaka, D. D. Johnson, I. Petrov, and J. E. Greene, Surf. Sci. **522**, 75 (2003).